Effects of predeformation on torsional fatigue in R260 rail steel

International Journal of Fatigue 179 (2024) 108031

Contents lists available at ScienceDirect

International Journal of Fatigue

journal homepage: www.elsevier.com/locate/ijfatigue

Effects of predeformation on torsional fatigue in R260 rail steel

Daniel Gren [a,*], Knut Andreas Meyer [b]

[a] Department of Industrial and Materials Science, Chalmers University of Technology, Gothenburg, 41296, Sweden
[b] Institute of Applied Mechanics, TU Braunschweig, Braunschweig, 38106, Germany

ARTICLE INFO

Keywords:
Torsional fatigue
Axial-torsion
Pearlitic steel
Large plastic deformation

ABSTRACT

Rolling contact loading induces severe plastic deformations and initiates cracks near the rail surface. Prevention of such rolling contact fatigue cracks requires a better understanding about the mechanical behavior of the deformed material in this region. Even so, current rail standards do not consider the plasticity-induced changes to mechanical behavior. They only evaluate the mechanical performance of virgin rail steels under uniaxial loading conditions, which is not representative for the material's performance after years of service. This study proposes a new method for fatigue life evaluation of deformed material under loading conditions similar to rolling contact loading. Both virgin and predeformed test bars with a circumferential notch were subjected to strain-controlled torsional fatigue loading to evaluate the influence of axial loading, predeformation, and torsional loading direction. Superimposed compressive axial loads increase the fatigue life without affecting the torque response. The predeformed test bars exhibited longer lives, an effect we attribute to the combination of different torque responses, hardening, and anisotropy.

1. Introduction

In service, the repeated rolling contact loading of rails causes the material to deteriorate over time. The small contact patch area, through which the wheel load is transferred, causes a very high contact pressure. In addition, frictional loads caused by e.g. traction, cornering, and braking generate shear stresses. If the frictional loads are high and the traffic predominantly unidirectional, then ratcheting occurs i.e. accumulation of shear strain [1]. The material close to the railhead becomes severely deformed, and its material properties and mechanical behavior are significantly changed due to work hardening and microstructure alignment, see e.g. [2–5]. Cracks are often initiated in the severely deformed layer [6,7]. These cracks typically propagates along the direction of the microstructure alignment in the severely deformed surface region under mixed mode loading. However, most fatigue tests reported in the literature have been conducted on undeformed material under uniaxial loading and this is not representative for the material performance after years of service. Understanding the material behavior of the severely deformed surface material is a key factor for mitigating rolling contact fatigue (RCF).

Pearlitic steels are the most widely used material for railway rails. Such steels offer a good combination of wear and strength with respect to cost and their properties can be tailored to fit the operating conditions. The material state in the top of the rail has previously been replicated by high pressure torsion (HPT) [8], equal channel angular pressing (ECAP) [9] and axial-torsion [3]. In these methods, the material is severely deformed by applying large shear deformation under large compressive hydrostatic stresses, similar to the contact loading at the rail surface. Wetscher et al. [9] deformed the pearlitic rail steel R260 by ECAP to three different equivalent shear strain levels ranging from 0.67 to 2. Later, even higher equivalent shear strains (up to $\gamma = 30$) were achieved in rail steel R260 by Kammerhofer et al. [10], Hohenwarter et al. [8] and Leitner et al. [11,12], by using HPT. The experimental results from these studies showed that the strength in terms of fracture toughness and fatigue crack propagation rate under mode I loading strongly correlate with the direction of microstructure alignment relative to the crack plane. The lowest strength was measured when the crack plane was parallel to the microstructure alignment, i.e. parallel to the cementite lamellae, and the highest strength when the crack plane was perpendicular to the microstructure alignment. The main limitation of ECAP and HPT as methods for replicating the severely deformed surface layer is that the extracted specimen size must be small for the material state to be well defined. Axi-symmetric test bars required for fatigue testing cannot be produced with ECAP and are very difficult to obtain with HPT. To overcome this limitation and enable fatigue testing Meyer et al. [3] developed a new method to replicate the material state at the rail surface by twisting cylindrical test bars under a compressive axial load. This method can reach shear strains up to 2.3. The replicated material corresponds to the material state at greater depths beneath the rail surface as compared to HPT, which can achieve larger shear strains.

* Corresponding author.
E-mail address: daniel.gren@chalmers.se (D. Gren).

https://doi.org/10.1016/j.ijfatigue.2023.108031
Received 24 August 2023; Received in revised form 19 October 2023; Accepted 31 October 2023
Available online 2 November 2023

Table 1
Nominal chemical composition of the R260 steel.

C	Si	Mn	P	S	Cr	Al	V	N	Cu
0.72	0.31	1.04	0.006	0.010	0.02	<0.002	<0.005	0.006	0.018

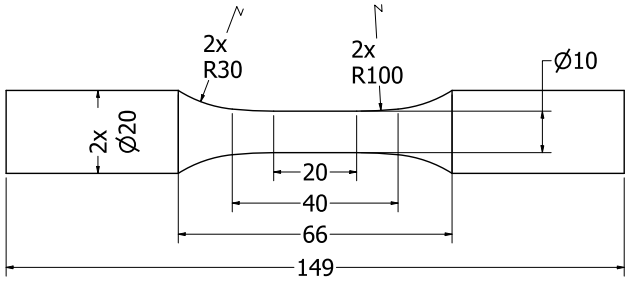

Fig. 1. Geometry and dimensions of the test bars used for predeformation in [mm].

Recently, Schnalzger et al. [13] conducted fatigue crack propagation experiments under mode II loading on pearlitic rail steel R260 using hollow cylindrical test bars. Solid cylindrical test bars were predeformed by the method proposed by Meyer et al. to $\gamma = 1.6$ and a new, modified HPT method to $\gamma = 3.5$. Coplanar crack growth was observed for the test bars predeformed by HPT. The crack followed the microstructure alignment and the crack propagation rate was higher at lower loads than the undeformed material and material predeformed by compression–torsion. Gren et al. [14] conducted stress-controlled uniaxial fatigue crack propagation experiments, predeformed to different levels by compression–torsion. It was reported that the crack propagation resistance of the predeformed material was higher than for the undeformed material. The increased crack propagation resistance was attributed to differences in plastic deformation whilst the effect of microstructure alignment was considered to be limited. The results from previous studies highlights the importance of fatigue testing in predeformed material. Fatigue crack propagation experiments of replicated surface material under strain-controlled cyclic torsional loading have not been conducted to the authors' knowledge. This study aims to investigate how previously accumulated shear strains affect the fatigue behavior during rolling contact-like loading by using test bars predeformed by compression–torsion. The study also aims to investigate how the direction of the applied shear load affects the fatigue behavior of the predeformed test bars.

2. Materials and methods

2.1. Material

Torsional fatigue crack initiation and early crack propagation in the pearlitic rail steel R260 have been studied. The microstructure is almost fully pearlitic with a nominal chemical composition according to Table 1. The material was received as cylindrical rods, extracted close to the railhead surface of virgin rails. Test bars were machined from these cylindrical rods with the geometry and dimensions from the drawing in Fig. 1.

2.2. Test bars

The material state close to the surface of highly deformed railheads was replicated with the predeformation method developed by Meyer et al. [15], as illustrated in Fig. 2a: test bars are repeatedly twisted 90° under a constant compressive force. In this study, the compressive force was set to give an initial nominal compressive stress of 500 MPa to prevent buckling and avoid premature failure during predeformation, following [15]. For this compressive stress, a detailed microstructural analysis was conducted by Nikas et al. [16], at deformation levels for 3 × 90° and 7 × 90°. During the initial method development for

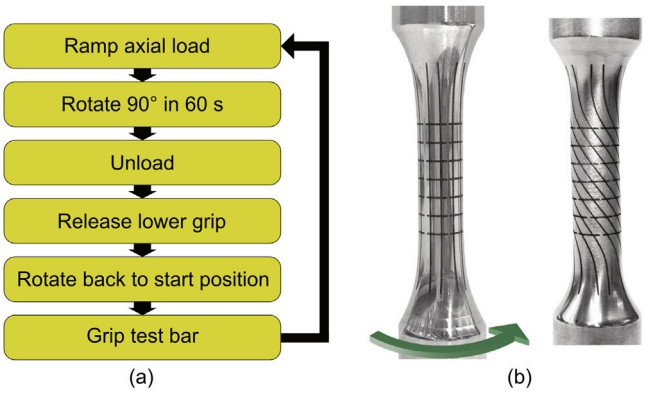

Fig. 2. Predeformation method. (a) flowchart of the predeformation process and (b) visualization of shear deformation resulting from twisting 3 × 90°.

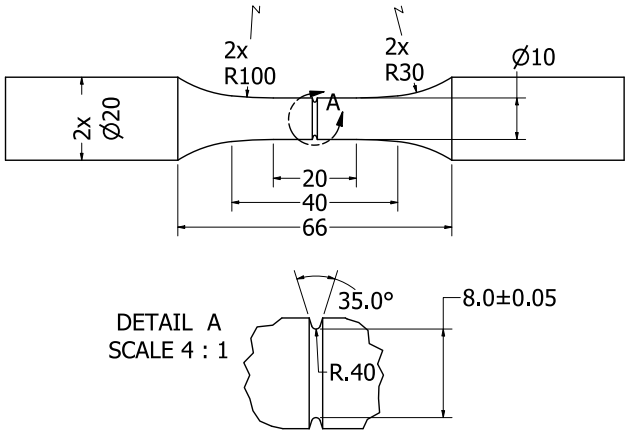

Fig. 3. Geometry and dimensions of undeformed and notched test bars.

the present study, we found a large scatter in the fatigue life after 6 × 90° predeformation steps. Therefore, one deformed material state, corresponding to twisting 3 × 90° (PD3) was investigated, see Fig. 2b. The direction of the torsional load (green arrow) during predeformation is throughout the paper denoted as loading along the direction of predeformation. The predeformation state denoted PD3 corresponds to the material state found just below the railhead surface. The exact distance depends on how severely deformed the railhead is. The servo-hydraulic axial-torsion system MTS 809, instrumented with a ±100 kN and ±1100 Nm load cell, and displacement and rotation ranges of ±75 mm and ±45°, was used for both predeformation and fatigue testing.

At the center of the gauge section, a circumferential notch were machined for all test bars, following the dimensions of the notch as specified by the drawing in Fig. 3. This figure shows the geometry and dimensions of the undeformed test bars. In the case of the predeformed test bars, where the length decreases and gauge section diameter increases due to predeformation, a new gauge section was first re-machined, symmetric at the center before machining the notches. The new gauge section had a gauge length of 40 mm and gauge diameter of 10 mm.

The geometry differences between the undeformed test bars and reprofiled predeformed test bars do not influence fatigue testing as the strains are measured across the notch where the geometries are identical. The gauge section was ground in steps to P1200 abrasive paper to remove the grooves from machining and make the surface suitable for the extensometer.

Gren et al. [14] measured the surface shear strain of PD3 test bars to 0.74 ± 0.05, which equates to a shear strain of 0.56 at the notch root of the predeformed test bars used in the present study.

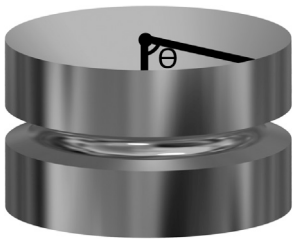

Fig. 4. Illustration of the rotation angle used for controlling the fatigue experiments.

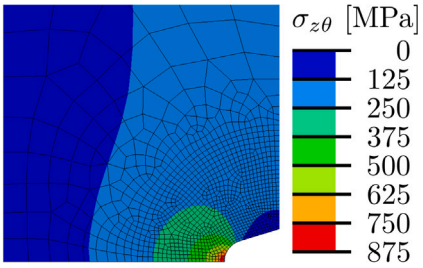

Fig. 5. Elastic shear stresses around the notch, simulated with finite elements for a 50 Nm torque.

Table 2
Test matrix.

Predeformation	Direction	Axial load	No. of test bars
PD0	Along	−100 MPa	3
PD0	Along	0 MPa	3
PD3	Along	−100 MPa	2
PD3	Along	0 MPa	2
PD3	Against	−100 MPa	2

2.3. Experimental

2.3.1. Design of experiments

The fatigue crack propagation experiments were conducted under pulsating cyclic loading in order to investigate the influence of load direction on the fatigue behavior of predeformed material. The fatigue experiments were strain controlled to avoid ratcheting which would have increased the loading difference between the material states and loading directions. The torsional strain was controlled by the rotation angle $\theta = 0.0132 \pm 0.0044$ [rad], measured by a biaxial extensometer (MTS 632.80F, +1.2/−0.5 mm, ±5°) over its gauge length $L = 12$ mm, as illustrated in Fig. 4. The waveform of the torsional load was sinusoidal and the frequency was set to 1 Hz. The strain interval was experimentally determined to achieve an initial torque response of 0 to 50 Nm for undeformed material, resulting in a similar effective nominal stress as in [14]. This loading gives a maximum elastic shear stress range about 850 MPa at the notch root and elastic shear strain of about 0.01, as shown by the Finite Element simulation results in Fig. 5. This analysis was performed using axisymmetric elements with twist (CGAX4R) in Abaqus, using 0.05 mm element to resolve the stress concentration. As this stress is far above the yield strength of the material, $R_{p0.2} = 534$ MPa, see Table 2 in [3], the actual shear strain is higher. The monotonic response in axial and shear loading for this material is presented in Figure 12 in [17] for different levels of predeformation, and the tensile loading up to 7% strain in Figure 2 in [18] (As-received R260). The plastic response is also visible for the torque-rotation results presented in Section 3.1.

The test matrix for the fatigue experiments is given in Table 2. The direction of the torsional load was either along or against the direction of predeformation, with or without a superimposed compressive axial load of −100 MPa. To investigate the fracture surface after fatigue testing the test bars were rapidly opened in tension.

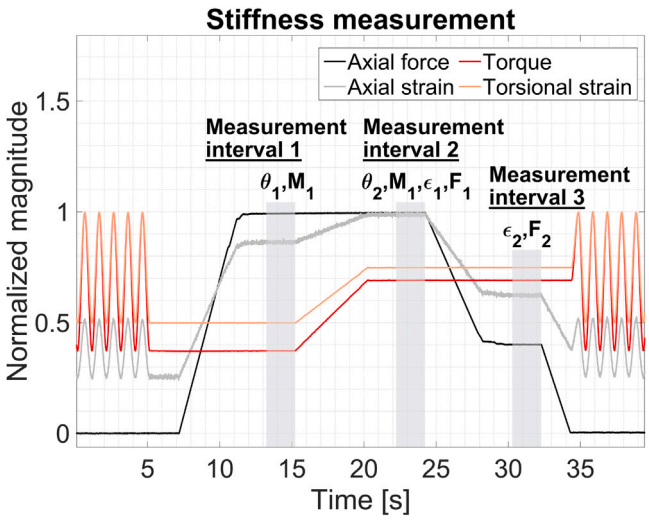

Fig. 6. Measurement of axial and torsional stiffness.

The second test of the load case where a PD3 test bar was subjected to torsional loading against the direction of predeformation was restarted after running a few cycles with a frequency of 1 Hz. The test became unstable and was therefore interrupted by the narrow strain limits set in the control software. To avoid further interruptions it was decided to make the test more robust by restarting the test at a lower frequency of 0.4 Hz.

2.3.2. Fatigue life definition

Axial and torsional stiffness were used as a comparative measurement of the material damage evolution during fatigue testing. This method is easy to implement, allows continuous measurements, and relates to changes in mechanical behavior. An alternative approach that can be used is potential drop as was done by Tanaka et al. [19] during torsional fatigue loading of notched test bars. This method requires careful calibration and is limited by electrical shortening between the fracture surfaces [20].

Stiffness measurements were conducted every 1000th cycle and the fatigue life was defined as the number of cycles until a 5% drop from the initial axial stiffness. The fatigue life was based on axial stiffness as the influence of crack face friction in the torsional stiffness measurement cannot be determined. Eqs. (1) and (2) define the torsional and axial stiffness, using the measured quantities described in Fig. 6. These quantities were time averaged under 2 s to reduce measurement noise.

$$\text{Torsional stiffness} = \text{abs}\left(\frac{T_1 - T_2}{\theta_1 - \theta_2}\right) \tag{1}$$

$$\text{Axial stiffness} = \text{abs}\left(\frac{F_1 - F_2}{\epsilon_1 - \epsilon_2}\right) \tag{2}$$

The torsional stiffness was measured under a nominal tensile stress of 50 MPa at θ_{min} and at θ_{m}. The axial load was applied to reduce the influence of crack face contact. At measurement intervals 1 and 2, the average magnitude of the torque, T, and the torsional rotation, θ, were measured. These magnitudes are denoted as T_1, T_2, θ_1 and θ_2 for respective measurement interval. The axial stiffness was measured in unloading at interval 2 and 3, between a tensile stress of 50 MPa and 20 MPa to avoid influence of plasticity. The lower limit of the axial force was set to 20 MPa to reduce the influence from crack closure. At each interval, the average force F and average strain ϵ were measured, denoted as F_1, F_2, ϵ_1, and ϵ_2.

The axial load applied during the stiffness measurements was chosen to be low to limit its influence on the fatigue life. Using such a

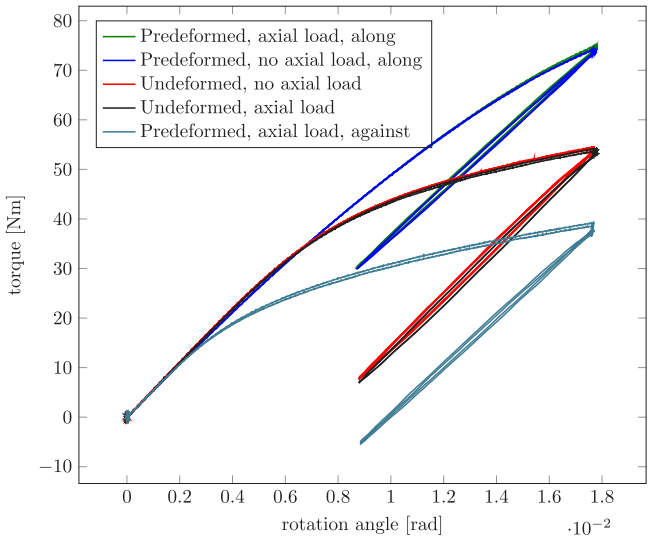

Fig. 7. Initial ramp and torsional load cycle for all load cases and material states.

low load implies small axial strains, making the axial stiffness measurements very sensitive to internal and external effects such as vibrations, temperature, and crack interactions. These issues were partly mitigated by time averaging before the stiffness calculation.

3. Results

3.1. Mechanical response

As previously mentioned, the torsional strain was controlled by the rotation angle $\theta = 0.0132 \pm 0.0044$ [rad] and the axial loading was load-controlled to give a nominal stress of either 0 or −100 MPa. Due to different stress–strain behavior, depending on predeformation state and loading direction, the torque response differs between the test cases. Consequently, the local stress state is not the same in each test case. The torque response during the initial ramp and the first load cycles are shown in Fig. 7. From the figure it can be seen that quite some plasticity occurs during the initial ramp. The following cycles display a small hysteresis, indicating a small amount of plasticity in each cycle, which is analyzed in more detail in Fig. 10.

Fig. 8 shows that all test bars have a similar torque range. The undeformed test bars have a slightly higher torque range due to their higher initial stiffness, as discussed in Section 3.2.

Fig. 9 shows the mean torque evolution. The mean rotation was chosen to give an almost pulsating torque for the undeformed test bars, resulting in the torque being approximately $20 \pm 22\ Nm$ for these cases. However, the mean torque differs between material states and loading directions. For loading against the predeformation direction, the absolute value of the mean torque is much lower than along. The latter gives a torque of approximately $45 \pm 22\ Nm$, while the former yields $T = -7 \pm 22\ Nm$. The influence of axial load on the torque response is negligible in comparison.

Rolling contact fatigue is often attributed to plastic deformations in the contact patch, cf. e.g. Johnson [21]. To observe differences in plasticity between samples, we investigate the accumulated work during the experiments, W. Below, we motivate that the major part of W is the plastic work. Thereafter, the accumulated work in Fig. 10 is presented.

The work, w_i, during a torsional cycle from time t_{i-1} to t_i is

$$w_i = \int_{t_{i-1}}^{t_i} \left[T\dot{\theta} + F\dot{u}\right] \mathrm{d}t \tag{3}$$

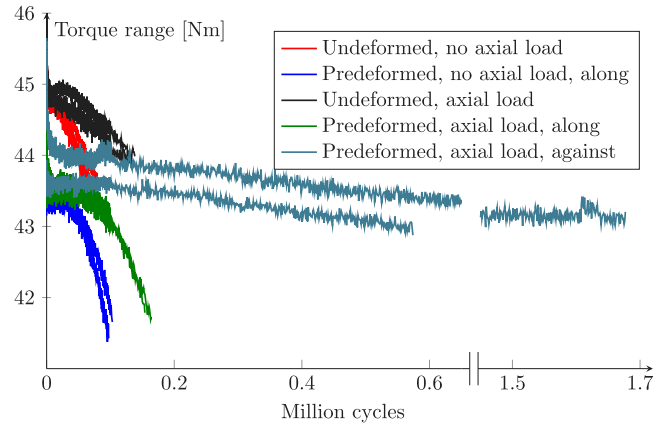

Fig. 8. Torque range for each test bar. The graph has been split for improved clarity. The torque range (predeformed, axial load, reversed) linearly decrease in between the split.

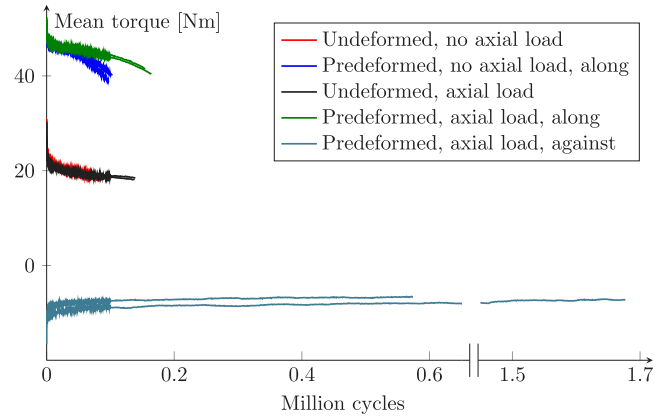

Fig. 9. Mean torque for each test bar. The graph has been split for improved clarity. The mean torque (predeformed, axial load, reversed) remains constant in between the split.

where T is the torque and θ is the rotation angle over the gauge length, $L = 12\,\mathrm{mm}$. The axial contributions are the force, F, and the axial displacement, u (change of L). However, as F is constant and u remains small, the axial contribution is negligible. Finally, the accumulated work, W, is then given as the sum of all cycles, $W = \sum w_i$.

For an elastic material, $w_i = 0$, as the torque, T, only depends on the rotation angle, θ, and $\theta\left(t_{i-1}\right) = \theta\left(t_i\right)$. Hence, w_i is a measure of the inelastic work in cycle i. In this section, we motivate why this inelastic work is primarily due to plastic deformations: The reversible elastic work from the valley to the peak is about $w_{\text{elastic}} = 0.36\ Nm$. In comparison, the inelastic work per cycle, w_i, is between 0.005 and 0.013 Nm after the first few cycles. Different sources contribute to the inelastic work, such as crack formation, crack face friction, and plastic deformations. The accumulated work due to crack formation under strain-controlled loading is limited to the elastic work in the first cycle. Hence, it must be less than $0.05 W_{\text{elastic}} \approx 0.02\ Nm$ due to the 5 % stiffness reduction. The inelastic work due to crack face friction is expected to be affected by the axial load, but no strong influence is observed. Furthermore, the work due to crack face friction should increase as damage evolve, but no such increase in inelastic work is observed. Based on these indications, we will assume that plasticity is responsible for most inelastic work.

In Fig. 10, no significant effects of axial forces or torsional direction are observed. The latter may seem inconsistent with the yield asymmetry reported in [17] that showed a lower yield limit in the reversed loading direction. However, those results only apply to the first loading after predeformation and not the cyclic response. Considering the

Table 3
Initial stiffness according to Eqs. (2) and (1) (average of first 10 measurements) and standard deviation between samples.

Direction	Undeformed	Predeformed	Unit
Axial	14.59 ± 0.05	14.27 ± 0.06	MN
Torsional	5.38 ± 0.02	5.06 ± 0.01	kNm

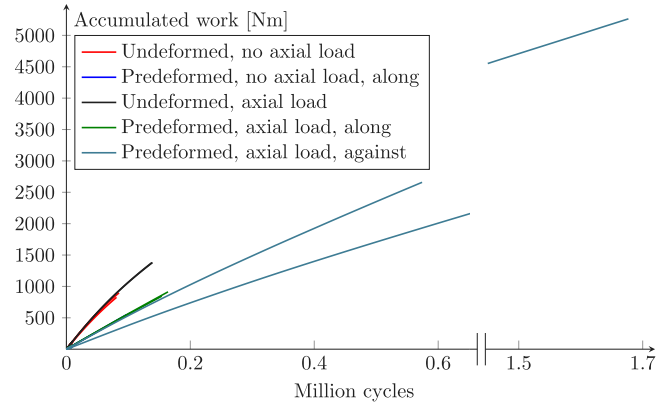

Fig. 10. Accumulated work, $W = \sum w_i$. The graph has been split for improved clarity. The accumulated plastic work (predeformed, axial load, reversed) increases linearly in between the split.

undeformed test bars, these have a higher work accumulation than the predeformed test bars. Fig. 8 showed that undeformed test bars had a higher torque range, which may seem contradictory to more plastic work. While those test bars have 6% higher torsional stiffness, the torque ranges after the first initial cycles are only 3% higher. This difference explains why the undeformed test bars experience more plastic deformations. Furthermore, the work in each cycle, w_i, is approximately constant for the predeformed test bars. For the undeformed test bars, w_i decreases during the experiment but remains higher than for the predeformed test bars.

In summary, the undeformed test bars sustain about twice the amount of accumulated plastic work compared to the predeformed bars after the same number of cycles.

3.2. Fatigue life evaluation

The initial stiffness of the undeformed and predeformed test bars, calculated as the average of the 10 first measurements are given in Table 3.

Compared to the predeformed material, the initial axial stiffness of the undeformed material is approximately 2% higher and the initial torsional stiffness is 6% higher. It was expected that the undeformed and predeformed material would have different initial stiffness. Meyer [17] measured the shear modulus and Young's modulus of both undeformed and predeformed tubular test bars of the pearlitic rail steel R260. It was reported that the shear modulus and Young's modulus of undeformed material were 3% respectively 1% higher than for material predeformed to $\gamma = 0.6$. The present study uses solid cylindrical test bars with a notch that induces an inhomogeneous stress field. In addition, the predeformed test bars have a shear strain gradient as opposed to the hollow test bars in [17]. Consequently, only the same qualitative differences in initial stiffness between undeformed and predeformed test bars are expected.

The stiffness measurements were filtered by a modified running average, as the standard running average will shift the data in the curvature direction. Each data point is calculated as the value predicted by a fitted 2nd order polynomial to 10 additional data points in both directions. With this method, the scatter for axial stiffness measurement was significantly reduced. Furthermore, no shift in the torsional

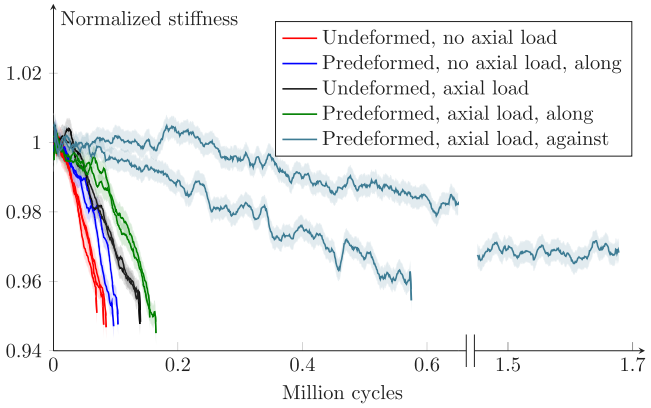

Fig. 11. Axial stiffness evolution for different material and loading conditions. The colored areas show ± one standard deviation. The graph has been split for improved clarity.

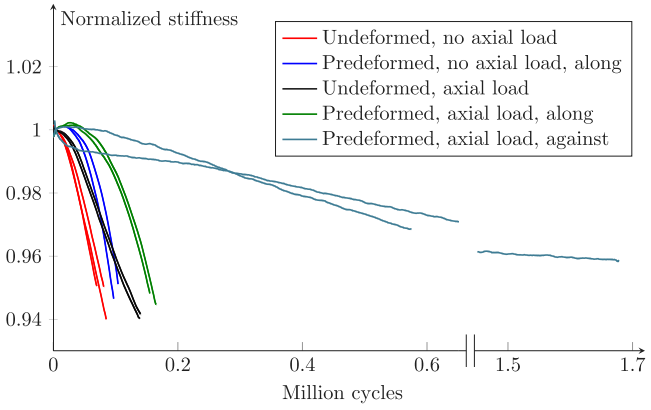

Fig. 12. Torsional stiffness evolution for different material and loading conditions. The graph has been split for improved clarity.

stiffness measurements was observed. The filtered axial and torsional stiffness measurements are presented in Figs. 11 and 12, respectively.

The axial stiffness measurements have a large scatter, as shown by the standard deviation (wrt. the difference between filtered and unfiltered data). For the torsional stiffness, the scatter is much lower and barely visible. This difference stems from the lower axial strain amplitude compared to torsional strain amplitude during the stiffness measurements. However, the variation between each repeated test is lower than the difference between different tests. The axial stiffness measurements are therefore sufficiently reliable. From Fig. 12 it is observed that torsional stiffness initially slightly increase for predeformed material. However, it cannot be seen in the axial stiffness measurements if this effect is present due to the measurement noise, see Fig. 11.

The fatigue life was longer for predeformed material and increased when a compressive axial load was applied. The compressive load influences the fatigue life more than the material state, and the effect was similar for both material states. Reversing the direction of the torsional load increased the fatigue life of the predeformed material the most. These results were unexpected as cracks then grow along the predeformed microstructure, see Section 3.3. This effect is further discussed in Section 4. It should be noted that the duplicate test endured more than three times the number of cycles. Moreover, due to computer memory constraints, the duplicate test was interrupted before a 5% reduction from initial axial stiffness was reached. Nevertheless, the trend is significant as also discussed in Section 4.

3.3. Fractography

The fracture surface was investigated for the different material states and loading conditions. The crack paths and shape of the fracture

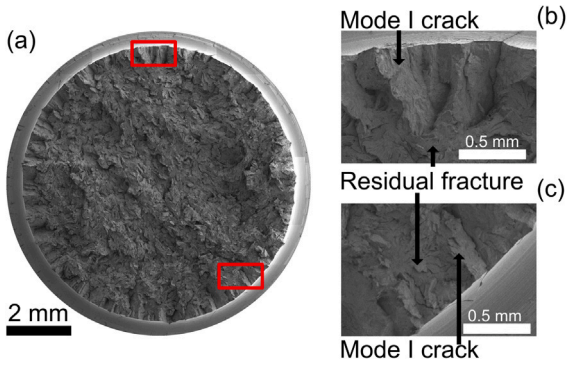

Fig. 13. Representative fracture surface of undeformed test bars cyclically shear loaded with and without a static compressive load. (a) overview, (b) and (c) detailed view.

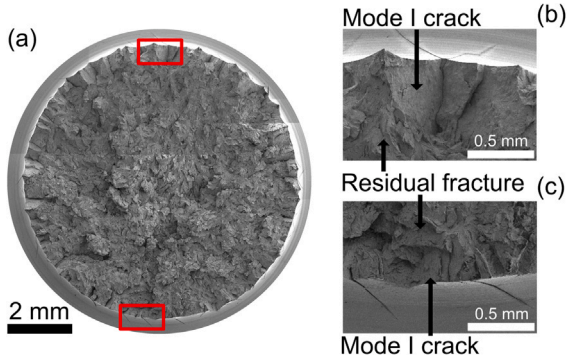

Fig. 14. Representative fracture surface of predeformed test bars cyclically shear loaded against the direction of predeformation with a static compressive axial load. (a) overview, (b) and (c) detailed view.

surface depend on the material state and loading condition. In all experiments, the fatigue zone represents the growth of multiple cracks initiated along the circumference of the notch. Moreover, the fatigue zone is characterized as a complex crack network. The crack growth plane varies around the circumference, and multiple cracks have grown beneath the observed fracture surface. In addition, the crack growth direction was observed to be either predominantly inclined clockwise or counterclockwise for torsional loads along respectively against the direction of predeformation. The fraction of cracks growing in the predominant direction was estimated by counting the cracks extending outside the notch. The cracks was observed to grow predominantly in Mode I according to the nominal stresses, as discussed in Section 4.1

The fracture surfaces of the undeformed samples, with and without a superimposed axial load appear similar. In Fig. 13, a representative fracture surface for undeformed samples is shown. The fatigue zone is mainly continuous with a rather uniform depth, but regions with no apparent fatigue cracking exist, see Fig. 13b and c. Characteristic for the fracture surface of undeformed material is the factory roof shape resulting from primarily mode I crack growth [19]. The factory roof is mainly asymmetric and the average fraction of cracks in the predominant direction was estimated to 65%.

The fracture surface of a predeformed sample subjected to torsional loading against the direction of predeformation is shown in Fig. 14. The fatigue zone is mainly continuous but not as uniform along the radial direction as for undeformed material. Similar to the undeformed material, the factory roof topology characterizes the fracture surface, for detailed view see Fig. 14b and c. The factory roof is mainly asymmetric and the average fraction of cracks in the predominant direction was estimated to 63%.

The fracture surface of predeformed test bars, subjected to torsional loading along the direction of predeformation, is markedly different

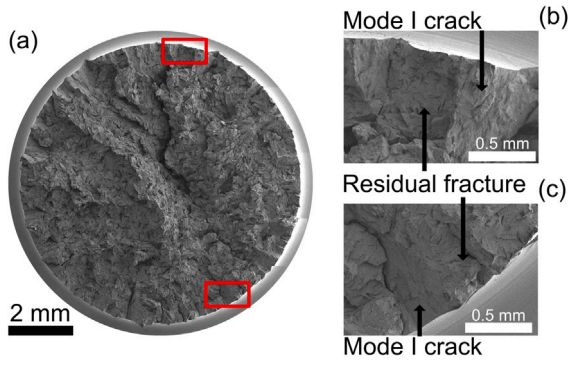

Fig. 15. Representative fracture surface of predeformed test bars cyclically shear loaded along direction of predeformation without a static compressive axial load. (a) overview, (b) and (c) detailed view.

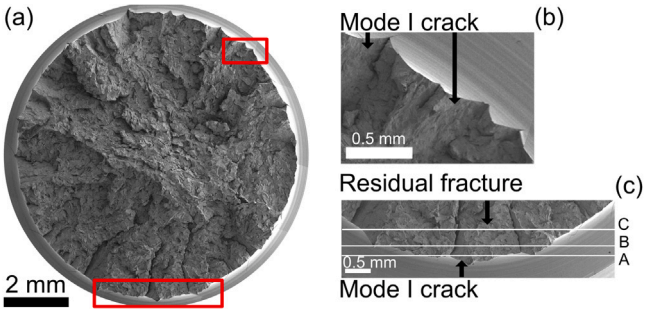

Fig. 16. Representative fracture surface of predeformed test bars cyclically shear loaded along the direction of predeformation with a static compressive axial load. (a) overview, (b) and (c) detailed view. The corresponding micrographs for the transverse sectioning lines in (c) are shown in Fig. 17.

from the fracture surface of the undeformed material. Representative fracture surfaces of predeformed material, without and with a compressive load, are shown in Figs. 15 and 16 respectively. The fatigue zones are heterogeneous and the crack path varies greatly around the circumference of the notch. The factory roof shape is not evident, instead, the fracture surfaces are characterized by a inclined crack growth in the clockwise direction. The fractions of cracks in the predominant direction were estimated to be 87% and 86% with, respectively without, an axial load.

The topography of the fracture surface does not capture the complete crack growth behavior as many cracks are concealed. The crack network was examined in more detail by transverse sectioning at different depths on the predeformed test bar in Fig. 16. The transverse lines A-C in Fig. 16c corresponds to the micrographs A-C in Fig. 17. The micrographs reveal crack growth underneath what is observed as a residual fracture on the topography. These cracks are observed to mainly grow against the direction of predeformation and thus along the direction of maximum remote principal stress, as illustrated and discussed in Section 4. In Appendix, the fracture surfaces of Figs. 13–16 are shown at an inclination angle of 50° to highlight surface topography and the notable difference between fatigue zone and residual fracture.

4. Discussion

4.1. Simplified analysis of predeformation and cyclic stress state

As reported in Section 3.2, a compressive axial load increases the fatigue life. This finding is in accordance with common fatigue life estimation models, see e.g. the Dang Van [22] (high cycle fatigue) and Jiang and Sehitoglu [23] (low cycle fatigue). The presented results show that the fatigue life is longer for predeformed test bars. The difference is very large when the loading direction is reversed compared

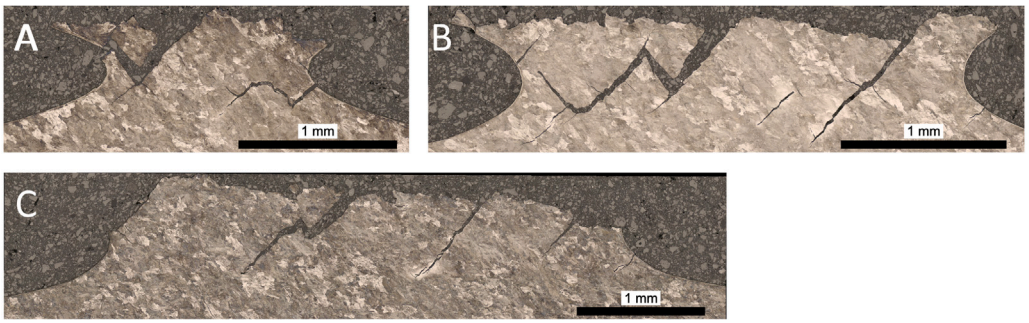

Fig. 17. Radial view of crack network of the predeformed test bar in Fig. 16 at different depths from the notch root (A) 51 μm (B) 234 μm (C) 547 μm.

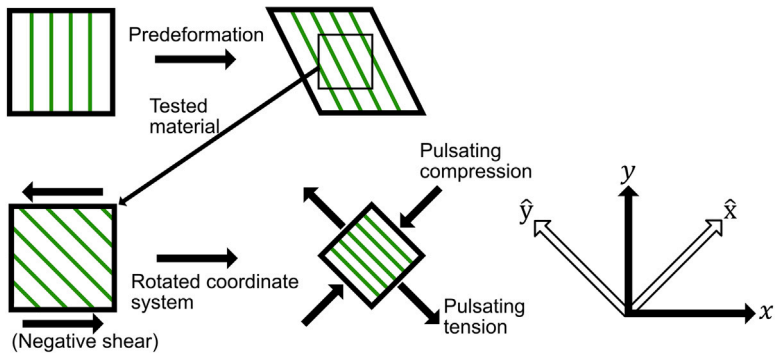

Fig. 18. Predeformation and cyclic stress state.

to the predeformation direction. To better understand the interplay of changes in material behavior, anisotropy and fatigue life, a simplified analysis of the predeformation and the cyclic stress state is presented first.

The bars are predeformed in the negative shear direction, as illustrated in Fig. 18. The initially vertical green lines slant to the left, illustrating the alignment of the microstructure (noting that the specific rotation angle is just for illustrative purposes). During testing, the material in the lower left is subjected to a negative shear strain for a positive torque (loading along with the predeformation direction). Without an axial load and for a uniform test bar, the principal stress directions are then inclined 45° (along $\hat{x}$ and $\hat{y}$) as illustrated in the lower right illustration. The stress magnitudes are then proportional to the applied torque. Hence, if the torque is positive and pulsating, $T = \Delta T \pm \Delta T$, the stress along the aligned microstructure is pulsating in tension. The stress transverse to the aligned microstructure is then pulsating in compression. Cracks with normal direction y are thus growing in Mode III, while cracks growing in the $\hat{y}$ and $\hat{x}$ directions are thus growing in Mode I. As observed on the fracture surfaces, and especially in Fig. 17, the cracks predominately grow in the inclined direction, i.e. Mode I.

Wetscher et al. [9] studied mode-I fatigue crack growth rates of the same R260 steel after Equal Channel Angular Pressing (ECAP) predeformation. They used Compact Tension (CT) samples in two different directions, one transverse to the microstructure alignment and one in the neutral direction. The latter corresponds to the radial direction in the present study.

Figure 7 in [9] shows crack propagation rates at different stress intensity factors, ΔK. For the present study, the samples after one ECAP pass (1A and 1B) are of particular interest since the predeformation shear strain, $\gamma = 0.67$, is similar to $\gamma = 0.56$ in the present study. For $\Delta K \in [7, 10]$ MPa $\sqrt{\text{m}}$, the transverse crack propagation rate (Sample 1B) was about twice that in the neutral direction (Sample 1A). Crack propagation relative the microstructure alignment in Sample 1B is comparable to the case in Fig. 18 for pulsating tension transverse to the microstructure alignment. Whilst when pulsating tension is along the microstructure alignment the crack grows along a more difficult path than in Sample 1A. Based on these results, it is expected that the life should be shorter for pulsating tension transverse to the microstructure alignment in Fig. 18. However, when the load direction was changed, a significantly longer life was observed.

As described in Section 2.3.1 the complementary test of the load case torsional loading against the direction of predeformation was restarted. The mechanical response as presented in Section 3.1 shows a similar mechanical behavior with only small differences in the torque range and mean torque. Whilst a notable difference is observed in the plastic work. Based on the similar mechanical response it is thought that the complementary test strengthens the finding that fatigue life strongly correlates with the direction of the applied load where torsional loading against the direction of predeformation significantly increases the fatigue life. However, as the test was restarted after several weeks with a lower frequency there exists a larger uncertainty in fatigue life as compared to the first test. It cannot however be concluded why a much longer fatigue life was observed in the complementary test as several factors can be contributing e.g. frequency dependence, static strain ageing and natural variability.

4.2. Effect of mean torque on crack path and fatigue life

While the torque ranges are similar for all test cases, the mean torque differs significantly between predeformation states and torsion directions. Considering the undeformed test bars, the approximate torque, $T \approx 20 \pm 22\ Nm$ gives the case depicted in the lower right part of Fig. 18 (without the aligned microstructure). The majority of the cracks in Fig. 13 grow in the $\hat{x}$ direction. As shown in Fig. 10, plastic deformations occur during the cyclic loading, which causes residual stresses. In combination with the notched sample geometry, this implies that the stress state is more complicated than that depicted in Fig. 18 which may explain why there are also cracks growing in the $\hat{y}$ direction.

For torsional loading in the predeformation direction, the fracture surfaces are very different from the other test cases. In this case, the mean torque is much higher, $T \approx 45 \pm 22\ Nm$, resulting in high

tensile stresses along $\hat{y}$ and high compressive stresses along $\hat{x}$. This will strongly promote crack growth in the $\hat{x}$ direction. However, the results in Wetscher et al. [9] show that crack growth is slower in this direction. This may partly explain why a longer life is observed in these predeformed cases despite a much higher tensile stress. The fracture surfaces in Figs. 15 and 16 also show much larger fatigue cracks along the $\hat{x}$ direction compared to the undeformed test bar in Fig. 13. These larger cracks result in a more irregular fracture surface. There are also very few cracks growing in the $\hat{y}$ direction.

When the torsional loading is reversed for predeformed test bars, a very different torque, $T = -7 \pm 22\ Nm$, is observed. In the simplified analysis above, such a torque response gives almost fully reversed tensile stresses in both $\hat{x}$ and $\hat{y}$ directions. Without an aligned microstructure, much longer fatigue lives can then be expected, if analyzed by using e.g. the Jiang–Sehitoglu [23] criterion. Even with the aligned microstructure, the same effect is clearly observed in the present study. The distribution of crack growth directions in Fig. 14 is, however, similar (but reversed) to the undeformed case. Hence, more cracks grow along the aligned microstructure than expected based on the stress state. This result is in accordance with the findings in [9].

The effect of mean torque has been investigated by Wang et al. [24] and McClaflin et al. [25] in isotropic medium carbon and high strength steel respectively. It was reported that mean shear stress has a detrimental effect on the fatigue life. The principal tensile stresses are highest for predeformed material subjected to torsional loading along the predeformation direction. Thus, the fatigue life should be shorter as compared to underformed material but the opposite was observed. Hence, we conclude that the predeformation extends the fatigue life for torsional loading in this direction. Loading against the direction of predeformation yields a much lower mean torque and based on the simplified stress analysis it should have the longest fatigue life which was also observed. Thus, it cannot be concluded whether predeformation has a beneficial effect when subjected to loading against the direction of predeformation.

4.3. Effect of residual stress and surface roughness

The residual stress state in the undeformed and predeformed test bars are different. In the case of the predeformed test bars, residual stresses are distributed across the entire cross-section [15]. Furthermore, the machining of the notches introduces further residual stresses, the magnitude of which may be affected by the different degrees of work hardening due to the predeformation. However, during the first loading cycle, all specimens undergo significant plastic deformations, see Fig. 7. These plastic deformations are likely to reduce, but not completely remove the differences in residual stresses between the material states. Consequently, in addition to the different macroscopic mean torque, unavoidable differences between the predeformation states may arise from local residual stresses.

The circumferential notches were machined using the same tool on a CNC machine. Since the amount of material removed for each notch is very small, it is reasonable to expect similar surface roughness for each test bar within the same material state. While minor differences may occur due to a different material hardness before and after predeformation, the plastic deformations in the first cycle will also alter the surface finish, and thereby reduce differences in surface finish between the samples.

4.4. Outlook for proposed method

The proposed method is suitable to evaluate fatigue of predeformed material during shear-dominated loading. In comparison to e.g. Wetscher et al. [9] and Schnalzger et al. [13], we observe a complex crack pattern. Our method is thus unsuitable to calibrate discrete crack propagation models. However, the results are useful to calibrate diffuse damage models, such as phase-field damage models (see e.g. Ambati et al. [26]). An additional advantage of the proposed method is the relatively simple sample preparation, not requiring hollow samples. This feature makes the method suitable to evaluate the performance of materials under predeformed conditions. Even though crack growth in rails occurs under predeformed conditions, such tests are not included in the rail material quality standard EN13674-1:2011 [27].

5. Conclusions

A new fatigue test method of rail steels under conditions similar to rolling contact loading, accounting for the large accumulated shear strains close to the surface, has been proposed. The method has been applied to investigate the influence of accumulated shear strains, compressive stresses, and loading direction in the R260 rail steel. The main findings are:

- The torque range is similar for all cases, within 41–45 Nm, but the mean torque depends on predeformation and load direction.
- A compressive axial load prolongs the fatigue life while having negligible influence on the torque. The increase by superimposing a compressive axial load is about 80% for undeformed material and 60% for predeformed material loaded along the direction of predeformation.
- The predeformed material sustains more cycles, about 12% and 27% with and without compressive axial load, respectively, for loading along the direction of predeformation, even though loading along the predeformation direction increases the mean torque.
- Loading against the predeformation direction increases the fatigue life even though cracks grow in a weaker microstructural direction. This result was attributed to the lower mean torque.
- The crack growth direction correlates strongly with the mean torque.
- Complex crack networks, similar to those observed in rail field samples, form around the notch.

CRediT authorship contribution statement

Daniel Gren: Conceptualization, Methodology, Software, Formal analysis, Investigation, Data curation, Visualization, Writing – original draft. **Knut Andreas Meyer:** Conceptualization, Methodology, Software, Formal analysis, Visualization, Writing – review & editing.

Declaration of competing interest

The authors declare that they have no known competing financial interests or personal relationships that could have appeared to influence the work reported in this paper.

Data availability

Data will be made available on request.

Acknowledgments

This work is a part of the activities within the Centre of Excellence CHARMEC (www.chalmers.se/charmec). They are funded within the European Unions's Horizon 2020 research and innovation programme in the Shift2Rail projects In2Track2 and In2Track3 under grant agreements No. 826255 and 101012456. The authors' would like to thank Professor Johan Ahlström at Chalmers University of Technology for the valuable discussions and input throughout the study.

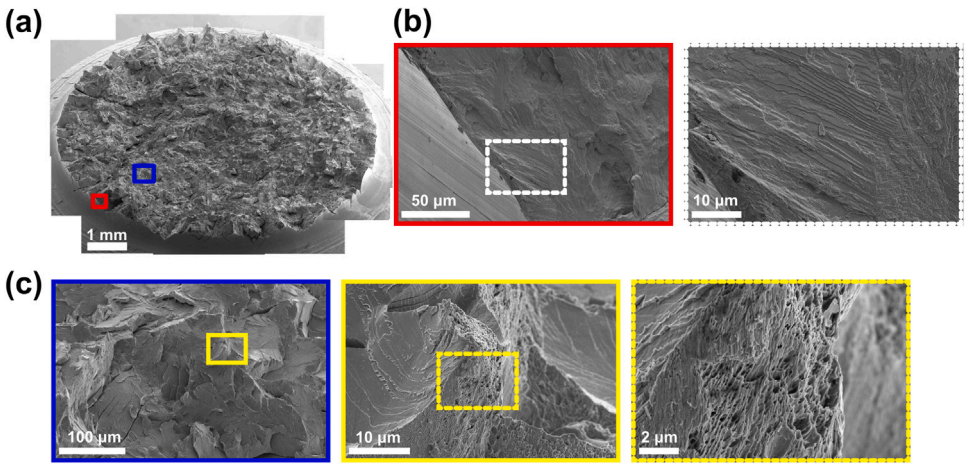

Fig. A.1. Representative fracture surface of undeformed test bars cyclically shear loaded with and without a static compressive load, same specimen as in Fig. 13. The scale bars apply to the x-direction. (a) overview, (b) detailed view of macroscopic mode I fracture (c) detailed view of residual fracture.

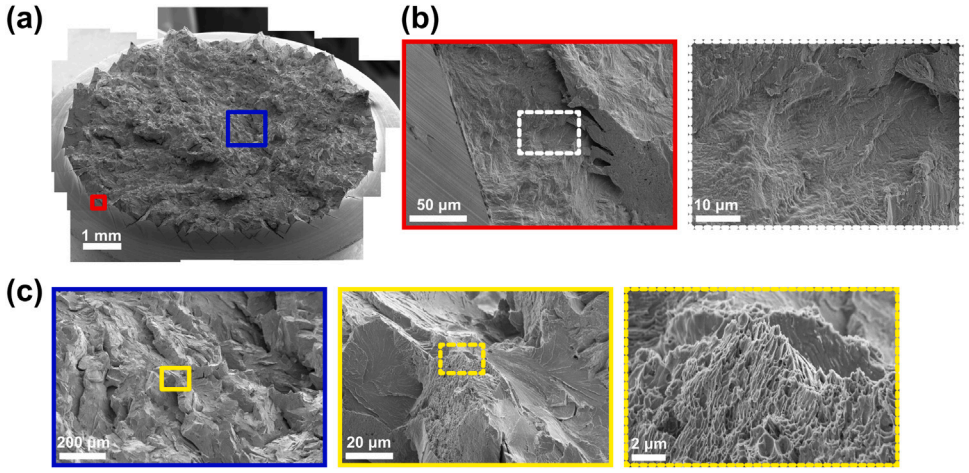

Fig. A.2. Representative fracture surface of predeformed test bars cyclically shear loaded against the direction of predeformation with a static compressive axial load, same specimen as in Fig. 14. The scale bars apply to the x-direction. (a) overview, (b) detailed view of macroscopic mode I fracture (c) detailed view of residual fracture.

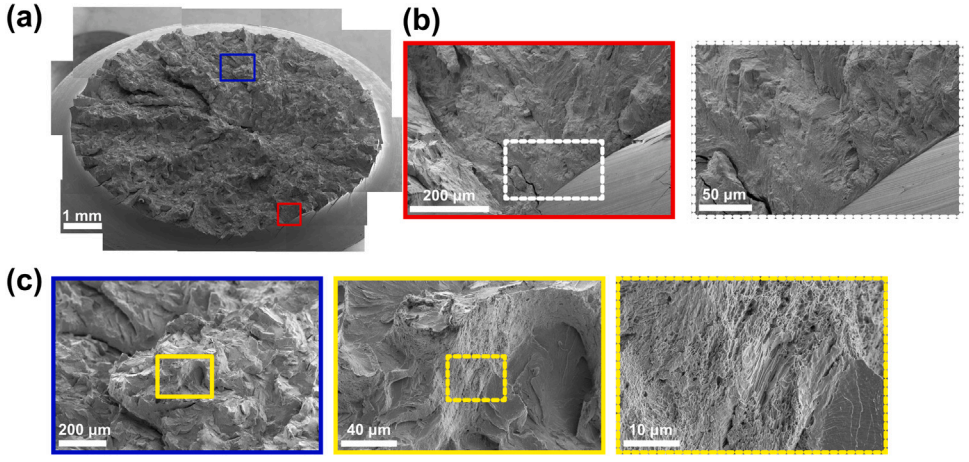

Fig. A.3. Representative fracture surface of predeformed test bars cyclically shear loaded along direction of predeformation without a static compressive axial load, same specimen as in Fig. 15. The scale bars apply to the x-direction. (a) overview, (b) detailed view of macroscopic mode I fracture (c) detailed view of residual fracture.

Appendix. Fracture surface

In Appendix, the fracture surfaces of Figs. 13–16 are shown at an inclination angle of 50° for a better overview of the 3 dimensional fracture surface, see Figs. A.1–A.4, both the typical fatigue fracture surface and residual fracture is detailed. The fatigue fracture surface is characterized by Mode I fracture and the residual fracture surface is mainly brittle failure but local areas of ductile fracture (dimples)

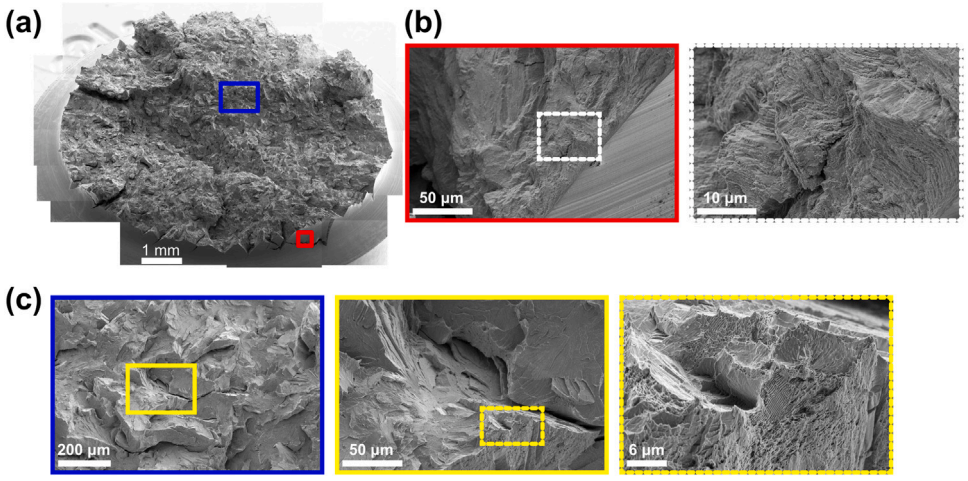

Fig. A.4. Representative fracture surface of predeformed test bars cyclically shear loaded along the direction of predeformation with a static compressive axial load, same specimen as in Fig. 16. The scale bars apply to the x-direction. (a) overview, (b) detailed view of macroscopic mode I fracture (c) detailed view of residual fracture.

can be observed. The fracture surface of the predeformed specimens loaded along the direction of predeformation is notably different from the undeformed specimens. The fatigue zone is heterogeneous and the fracture surface is rougher.

References

[1] Ekberg A, Kabo E. Fatigue of railway wheels and rails under rolling contact and thermal loading—an overview. Wear 2005;258(7):1288–300. http://dx.doi.org/10.1016/j.wear.2004.03.039, Contact Mechanics and Wear of Rail/Wheel Systems.

[2] Muster H, Schmedders H, Wick K, Pradier H. Rail rolling contact fatigue. The performance of naturally hard and head-hardened rails in track. Wear 1996;191(1):54–64. http://dx.doi.org/10.1016/0043-1648(95)06702-7, 4th International Conference on Contact Mechanics and Wear of Rail-Wheel Systems.

[3] Meyer KA, Nikas D, Ahlström J. Microstructure and mechanical properties of the running band in a pearlitic rail steel: Comparison between biaxially deformed steel and field samples. Wear 2018;396–397:12–21. http://dx.doi.org/10.1016/j.wear.2017.11.003.

[4] Schilke M, Larijani N, Persson C. Interaction between cracks and microstructure in three dimensions for rolling contact fatigue in railway rails. Fatigue Fract Eng Mater Struct 2014;37(3):280–9. http://dx.doi.org/10.1111/ffe.12112.

[5] Eden HC, Garnham JE, Davis CL. Influential microstructural changes on rolling contact fatigue crack initiation in pearlitic rail steels. Mater Sci Technol 2005;21(6):623–9. http://dx.doi.org/10.1179/174328405X43207.

[6] Fletcher DI, Franklin FJ, Kapoor A. Rail surface fatigue and wear. In: Wheel-rail interface handbook. Elsevier Ltd; 2009, p. 280–310. http://dx.doi.org/10.1533/9781845696788.1.280.

[7] Zerbst U, Mädler K, Hintze H. Fracture mechanics in railway applications—an overview. Eng Fract Mech 2005;72(2):163–94. http://dx.doi.org/10.1016/j.engfracmech.2003.11.010, Fracture Mechanics in Railway Applications.

[8] Hohenwarter A, Taylor A, Stock R, Pippan R. Effect of large shear deformations on the fracture behavior of a fully pearlitic steel. Metall Mater Trans A 2010;42:1609–18. http://dx.doi.org/10.1007/s11661-010-0541-7.

[9] Wetscher F, Stock R, Pippan R. Changes in the mechanical properties of a pearlitic steel due to large shear deformation. Mater Sci Eng A 2007;445–446:237–43. http://dx.doi.org/10.1016/j.msea.2006.09.026.

[10] Kammerhofer C, Hohenwarter A, Scheriau S, Brantner H, Pippan R. Influence of morphology and structural size on the fracture behavior of a nanostructured pearlitic steel. Mater Sci Eng A 2013;585:190–6. http://dx.doi.org/10.1016/j.msea.2013.07.032.

[11] Leitner T, Trummer G, Pippan R, Hohenwarter A. Influence of severe plastic deformation and specimen orientation on the fatigue crack propagation behavior of a pearlitic steel. Mater Sci Eng A 2018;710:260–70. http://dx.doi.org/10.1016/j.msea.2017.10.040.

[12] Leitner T, Hohenwarter A, Pippan R. Anisotropy in fracture and fatigue resistance of pearlitic steels and its effect on the crack path. Int J Fatigue 2019;124:528–36. http://dx.doi.org/10.1016/j.ijfatigue.2019.02.048.

[13] Schnalzger G, Werner D, Pippan R, Maierhofer J, Hohenwarter A. Crack path investigations in a pearlitic rail steel after pre-deformation under cyclic mode-II loading. Eng Fail Anal 2022. http://dx.doi.org/10.1016/j.engfailanal.2022.106567.

[14] Gren D, Ahlström J. Fatigue crack propagation on uniaxial loading of biaxially predeformed pearlitic rail steel. Metals 2023;13(10). http://dx.doi.org/10.3390/met13101726.

[15] Meyer KA, Ekh M, Ahlström J. Modeling of kinematic hardening at large biaxial deformations in pearlitic rail steel. Int J Solids Struct 2018;130–131:122–32. http://dx.doi.org/10.1016/j.ijsolstr.2017.10.007.

[16] Nikas D, Zhang X, Ahlström J. Evaluation of local strength via microstructural quantification in a pearlitic rail steel deformed by simultaneous compression and torsion. Mater Sci Eng A 2018;737:341–7. http://dx.doi.org/10.1016/J.MSEA.2018.09.067.

[17] Meyer KA, Ekh M, Ahlström J. Anisotropic yield surfaces after large shear deformations in pearlitic steel. Eur J Mech A Solids 2020;82:103977. http://dx.doi.org/10.1016/j.euromechsol.2020.103977.

[18] Meyer KA, Ahlström J. The role of accumulated plasticity on yield surface evolution in pearlitic steel. Mech Mater 2023;179:104582. http://dx.doi.org/10.1016/j.mechmat.2023.104582.

[19] Tanaka K. Crack initiation and propagation in torsional fatigue of circumferentially notched steel bars. Int J Fatigue 2014;58:114–25. http://dx.doi.org/10.1016/j.ijfatigue.2013.01.002.

[20] Ritter MA, Ritchie RO. On the calibration, optimization and use of DC electric potential methods for monitoring mode III crack growth in torsionally-loaded samples. Fatigue Fract Eng Mater Struct 1982;5(1):91–9. http://dx.doi.org/10.1111/j.1460-2695.1982.tb01227.x.

[21] Johnson K. The strenght of surfaces in rolling contact. J Mech Eng Sci 1989;203(December 1988):151–63.

[22] Dang-Van K. Macro-micro approach in high-cycle multiaxial fatigue. In: Mcdowell DL, Ellis R, editors. ASTM special technical publication. 1993, p. 120–30. http://dx.doi.org/10.1520/STP24799S.

[23] Jiang Y, Sehitoglu H. A model for rolling contact failure. Wear 1999;224(1):38–49. http://dx.doi.org/10.1016/S0043-1648(98)00311-1.

[24] Wang CH, Miller KJ. The effect of mean shear stress on torsional fatigue behavior. Fatigue Fract Eng Mater Struct 1991;14(2–3):293–307. http://dx.doi.org/10.1111/j.1460-2695.1991.tb00659.x.

[25] McClaflin D, Fatemi A. Torsional deformation and fatigue of hardened steel including mean stress and stress gradient effects. Int J Fatigue 2004;26(7):773–84. http://dx.doi.org/10.1016/j.ijfatigue.2003.10.019.

[26] Ambati M, Gerasimov T, De Lorenzis L. A review on phase-field models of brittle fracture and a new fast hybrid formulation. Comput Mech 2015;55(2):383–405. http://dx.doi.org/10.1007/s00466-014-1109-y.

[27] EN13674-1. Railway applications - track - rail - part 1: Vignole railway rails 46 kg/m and above. Brussels: European Committee for Standardization; 2011.